CIRP Journal of Manufacturing Science and Technology 69 (2026) 230–242

Contents lists available at ScienceDirect

CIRP Journal of Manufacturing Science and Technology

journal homepage: www.elsevier.com/locate/cirpj

Full-length article

Feeling machines: Prediction of thin-walled workpiece deflection by monitoring variations in tool bending moment pattern during circumferential milling

Michel Kenneth Seiffert *, Sebastian Junghans, Lasse Evers, Jan Hendrik Dege

Institute of Production Management and Technology, Hamburg University of Technology, Denickestraße 17, 21073, Hamburg, Germany

ARTICLE INFO

Keywords:
Milling
Workpiece deflection
Thin-walled workpiece
Sensor
Error compensation

ABSTRACT

In circumferential milling, the in-process deflection of thin-walled workpieces induced by feed normal forces results in reduced material removal, leading to geometric errors after machining. With the increasing use of additive manufacturing technologies and the production of near-net-shape structures, this problem is gaining increasing importance. Various strategies attempt to compensate for this geometric errors, for example by modeling the occurring cutting forces and workpiece deflection and then applying countermeasures during machining. However, this requires a high level of process understanding, and multiple parameters need to be considered, including material properties, cutting edge geometry as well as wear state of the tool. This paper examines a novel approach to predict workpiece deflection state by analyzing the bending moment pattern measured by an in-process sensor system located in the tool holder. It could be demonstrated that features extracted and evaluated from the bending moment signal can represent the current deflection state of the workpiece in an offline approach, enabling future in-situ toolpath adaptation to reduce geometric errors without relying on time-consuming simulation of the workpiece stiffness and with minimal signal processing effort.

1. Introduction

Thin-walled structures are becoming increasingly important not only in the aerospace industry but also across various lightweight design applications [1]. At the same time, rising demands for energy and resource efficiency in industrial production are pushing manufacturers to optimize processes while maintaining high part quality [2,3]. The issue is particularly critical when machining expensive and hard to machine materials such as titanium alloys. Although titanium provides an excellent strength-to-weight ratio as well as corrosion and high-temperature resistance, it imposes significant challenges when machining. Its low thermal conductivity and high tensile strength lead to rapid tool wear and high process forces.

In this context, additive manufacturing offers a promising alternative to conventional machining processes by enabling the near-net-shape production of titanium components. It involves building up parts layer by layer, placing material only where it is needed. As a result, less material needs to be removed compared to machining from solid stock, which lowers energy consumption, improves material utilization and reduces tooling costs. One suitable field of application is aircraft structural components, which often consist of numerous thin-walled stiffening ribs that are only a few millimeters thick. For the manufacturing of an example component weighing 0.56 kg, as shown in Fig. 1b, the use of a hybrid additive–subtractive process (Fig. 1c) reduced chip waste to 2.2 kg, compared to 24.6 kg machined in a fully subtractive process (Fig. 1a).

To achieve the required geometric and surface tolerances and to remove any possible remaining support structures, additively manufactured parts require a final subtractive machining step [4]. Circumferential milling is often used to machine surfaces with high productivity. As these parts are close to their final shape and therefore very thin from the beginning, a major challenge when machining compliant, thin-walled parts is their deflection under process forces, as illustrated in Fig. 2 [5]. When the workpiece deflects away from the tool, the width of cut a_e decreases, which reduces material removal and causes a geometric error once the part springs back after machining. The issue is especially critical for additively manufactured parts, which are highly compliant due to their near-net-shape.

Milling strategies for reducing this deflection induced geometric error can be divided into two groups: *Process-related strategies* and

* Corresponding author.
E-mail address: michel.seiffert@tuhh.de (M.K. Seiffert).
URL: https://www.tuhh.de/ipmt/das-ipmt/team/ms (M.K. Seiffert).

https://doi.org/10.1016/j.cirpj.2026.06.004
Received 15 December 2025; Received in revised form 7 May 2026; Accepted 21 June 2026
Available online 30 June 2026

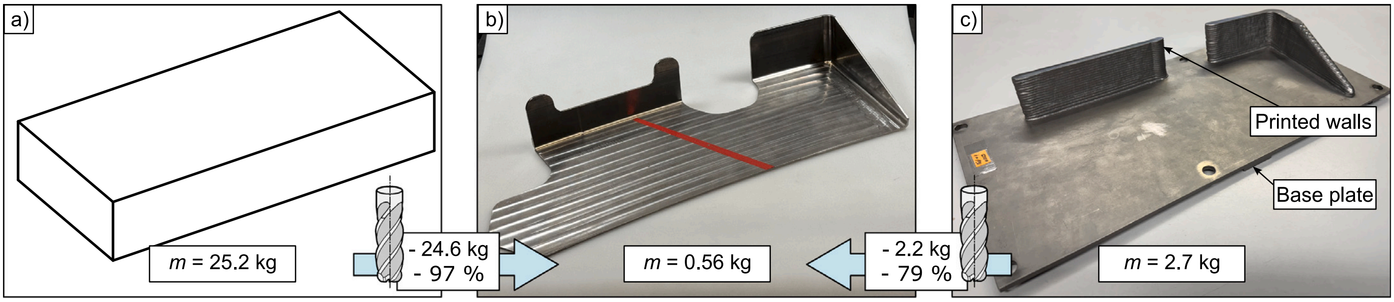

Fig. 1. Comparison between conventional and hybrid additive–subtractive manufacturing of an aircraft structural component (Ti-6Al-4V): (a) Solid raw part; (b) final machined part; (c) additive manufactured part before final machining.

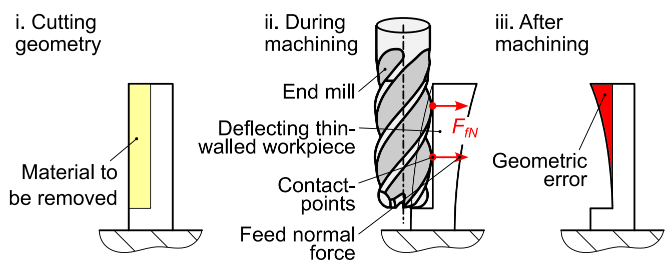

Fig. 2. Geometric error formation due to deflection of thin-walled workpieces, shown in cross-section.

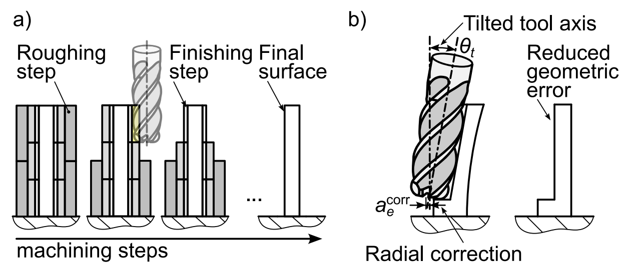

Fig. 3. Milling strategies to reduce the geometric error: (a) Multi-step machining to limit workpiece deflection (*waterline milling*); (b) Toolpath adaptation to mirror workpiece deflection.

compensation strategies [6]. The aim of *process-related strategies* is to minimize the deflection of the workpiece by reducing the mechanical loads. A common approach is the so-called *waterline milling* in Fig. 3a, where the thin-walled part is machined in multiple steps, with the width and depth of cut being reduced as the final shape is approached. The depths of cut are selected to ensure that the process forces, especially the feed normal force, remain small in relation to the workpiece's local compliance. For this method, productivity losses must be taken into account due to multiple machining steps and the reduced material removal rate. Furthermore, the tool's full potential (axial depth of cut) is not used, leading to an uneven tool wear along the cutting edge. *Compensation strategies*, on the other hand, allow the workpiece to deflect while simultaneously correcting the resulting error through adaptation of the toolpath. Fig. 3b illustrates how the tool's rotation axis is tilted by a tilt angle θ_t and how the width of cut a_e is adjusted via a width of cut correction a_e^{corr} to account for workpiece deflection and reduce the resulting geometric error. Since fewer machining steps are required due to the higher axial depth of cut compared to *waterline milling*, this strategy significantly improves productivity and makes full use of the end mill's length, resulting in more even wear along the cutting edge. To compute an adapted toolpath that minimizes geometric error, the workpiece deflection occurring during machining must be known in advance. This can be determined either through labor-intensive measurements of the geometric error after machining or via simulation-based deflection prediction models, which must account for numerous parameters such as tool wear, material properties, specific cutting coefficients or changing workpiece stiffness due material removal. However, both approaches can lead to an unfavorable cost–benefit ratio, which remains a major obstacle to widespread industrial adoption, especially when machining small-batch parts [7].

With the recent increase in publications and advances in sensor technology, a promising approach is to integrate sensors like force, torque, displacement, acceleration and temperature sensors into the machining process to collect real-time process data [8]. The data can then used to monitor and adapt the machining process in real-time. Denkena et al. go so far as to introduce the term “feeling machines”, emphasizing the ability of machines to monitor and adapt to their environment [9]. Compared to simulation-based approaches, which must account for numerous parameters to achieve the desired precision, evaluating in-situ sensor data offers the advantage that disturbances in the machining process can be directly observed in the data measurements. The main task in evaluating sensor data is identifying which features correspond to the phenomena that need to be monitored — in this article, the deflection of the workpiece. The challenge in integrating sensor systems is the limited available space, as it is desirable to position the sensors as close as possible to the tool engagement point so that the signal is not disturbed by unwanted noise or attenuated through damping [8].

Previous efforts for the prediction and compensation of such errors are summarized in the following. Denkena and Boujnah present the development of “sensing machine tools” for real-time detection and compensation of tool deflection in milling processes [10]. Conventional compensation approaches are either model-based, suffering from limited accuracy, or rely on external force measurement systems that restrict the machine workspace and are therefore of limited industrial applicability. To overcome these limitations, Denkena and Boujnah integrated strain gauges directly into stiff machine tool components such as the spindle head. Due to the high structural stiffness, the resulting strain signals are very small, which is addressed by local geometric modifications (e.g. notches) that increase strain sensitivity by up to 300% with negligible stiffness reduction. In addition, thin-film strain gauges are used to improve signal quality, while disturbance effects such as gravity-induced deformations are compensated in real time using polynomial correction models. The tool deflection is estimated by combining measured cutting forces with the identified tool stiffness, which is obtained through an automated calibration procedure based on controlled tool–workpiece contact. Experimental results show that the estimated deflection correlates well with measured workpiece deviations, with errors below 10 μm. Two compensation strategies are evaluated: adaptive feed control and real-time trajectory offset. While feed control improves form accuracy by around 70% at the expense of productivity, trajectory compensation achieves up to 80% improvement without reducing machining time. Overall, the study demonstrates the feasibility of structurally integrated sensing for accurate and industrially viable real-time compensation of tool deflection in milling.

Ratchev et al. present an integrated simulation environment for predicting and compensating machining errors in low-stiffness components, such as thin-walled aerospace parts [11]. The approach addresses the problem that conventional CAD/CAM systems assume rigid workpieces and therefore cannot capture elastic deformations induced by cutting forces, which lead to significant deviations between nominal and actual part geometry. The proposed framework couples multiple models within a unified, object-oriented data structure: an analytical cutting force model, a finite element analysis (FEA) module implemented via ABAQUS and a voxel-based material removal model. The cutting force and workpiece deflection are strongly interdependent, requiring an iterative solution strategy in which forces and deformations are repeatedly updated until convergence is reached. Validation experiments on an aluminum thin-walled workpiece demonstrate good agreement between predicted and measured deflections, with convergence typically achieved after a small number of iterations. The study highlights that the highest deviations occur at tool entry and exit regions due to transient cutting conditions. Overall, the work demonstrates the feasibility of integrating analytical, numerical and geometrical models within a unified simulation environment to improve prediction accuracy for flexible workpieces, while also highlighting the computational cost associated with iterative force–deformation coupling.

An approach to utilizing sensory information to adapt the milling process is by Denkena et al. to compensates for tool deflection by utilizing the drive signals of a milling center [12]. First, static process forces are reconstructed based on the drive signals. Then, using a stiffness model of the tool, the tool deflection is calculated, which leads to geometric errors during machining. Finally, a controller is designed to minimize geometric errors via either feed override control or positional control. Another noteworthy approach is proposed by Evers et al. who used two eddy current sensors to measure the in situ deflection of the workpiece [13]. The eddy current sensors were mounted on the spindle, allowing them to travel along behind the thin-walled workpiece during machining. The sensor signals are then used in a control loop to adjust the toolpath and adapt the width of cut to the measured deflection. This enables the finishing of near-net-shape workpieces while maintaining high material removal rates. In the study by Alzugaray-Franz et al. an acoustic emission sensor that is mounted close to the workpiece clamping is used for the online estimation of cutting parameters [14]. The proposed method involves extracting time-based features from the signal to estimate the width and depth of cut by identifying transitions between cutting phases from the corresponding waveforms.

When it comes to machining thin-walled, near-net-shape workpieces that are prone to deflection, there is still a noticeable gap in the available sensor approaches found in the literature. Some approaches do exist, such as the work of Luo et al. [15]. In their method, a thin-film polyvinylidene fluoride (PVDF) sensor is attached to the non-machining surface of the thin-walled workpiece. Based on an experimentally derived relationship between the measured voltage and the corresponding deflection, the workpiece deformation can be monitored in real time during machining. This enables both vibration and deflection tracking.

However, existing approaches for monitoring and predicting the deflection of thin-walled workpieces or even tool deflection still exhibit several limitations. Methods based on sensors attached directly to the workpiece require additional manual preparation, may introduce collision risks during machining and often suffer from reduced signal quality for large workpieces due to increased transmission distances when the tool moves along the workpiece. Other approaches require sensor systems to move together with the machining process, which increases collision risk, limits the applicable milling strategies and must additionally be considered during CAM programming. In addition, the prediction of deflections during machining of thin-walled components by extensive simulations remains challenging due to the tight coupling between cutting forces and workpiece deformation. Workpiece deflection changes the local engagement conditions, which in turn alters the cutting forces and again influences the deformation state. This is especially challenging for large near-net-shape components that are produced only in very small batch sizes. Consequently, there remains a need for a sensing and signal evaluation approach that can identify workpiece deflection directly during machining without interfering with the machining process, while avoiding extensive iterative simulations, cutting force coefficients, or detailed FEM-based compliance models. Such a sensing system should not introduce additional collision risks, restrict toolpath strategies or increase the complexity of CAM programming. In particular, approaches requiring sensors mounted directly on the workpiece are impractical for large components or frequently changing geometries, as they require additional manual preparation and increase setup time. A promising alternative is the integration of the sensing system into the rotating tool holder, which requires robust wireless data transmission and reliable onboard power supply under machining conditions. Such sensor systems are already commercially available and used in industrial applications, making them a promising basis for in-process deflection monitoring [16]. Furthermore, low latency and near real-time capability are essential requirements in order to enable future adaptive toolpath correction during machining. At the same time, the extracted signal features must remain robust against process disturbances such as tool runout, chatter and process noise.

The remainder of this paper is structured as follows. In Section 2.1, the general methodology for predicting workpiece deflection based on the analysis of the bending-moment signal is introduced. Therefore, Section 2.2 presents a simplified bending-moment calculation at the reference point on the tool holder. The purpose is to establish the physical understanding of the bending-moment signal and to derive the relationship between characteristic signal features and the effective width of cut $a_{e,\mathrm{eff}}$. In Section 2.3, process data are collected using a sensor-integrated tool holder, followed by several signal post-processing steps. Section 3 then visualizes how characteristic features in the bending-moment signal change with varying process parameters. The model is compared with the measured and post-processed process data and the workpiece deflection is predicted directly from the measured signal features. Finally, Section 4 summarizes the main findings of the study and discusses future work towards in-situ compensation of workpiece deflection and adaptive toolpath adjustment.

2. Methodology

2.1. Approach for predicting workpiece deflection

The approach in this paper to predict workpiece deflection extends the work of Choi et al. [17], in which the depth of cut a_p in circumferential milling was predicted based on cutting forces measured by a stationary force measurement platform. Since the proposed algorithm relies on the cutting force pattern rather than its absolute magnitude, the effects of variations in cutting conditions and tool wear can be effectively excluded.

The proposed approach is extended to predict changes in the width of cut a_e resulting from the deflection of thin-walled workpieces. This is accomplished by analyzing variations in the bending moment pattern measured by a process-integrated sensor system, as illustrated in Fig. 4. The bending moment caused by the process forces is measured using strain gauges integrated into the tool holder arranged 90° apart around the circumference and transmitted wirelessly via a transmitter–receiver unit. This enables measurements to be taken in close proximity to the cutting zone, thereby minimizing the influence of external disturbances on the signal. The space-saving placement of the sensor within the tool holder, combined with wireless data transmission that eliminates the need for cable connections through the spindle, enables seamless integration into existing industrial applications. The strain gauges are

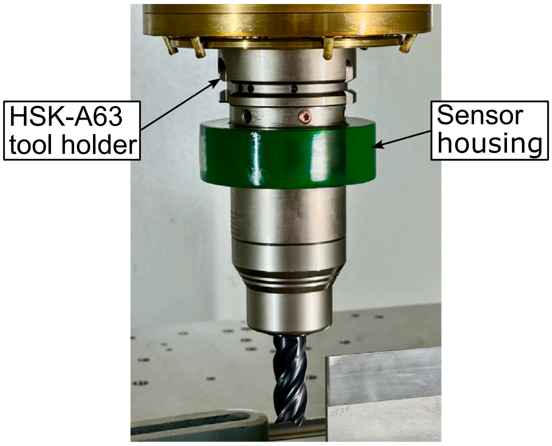

Fig. 4. Wireless, process-integrated sensor system for measuring bending moments used in this paper.

designed for a specific force range, which in this paper corresponds to a maximum bending moment of $M_b^{max} = 240\,\mathrm{N\,m}$. They are embedded in plastic to protect them from coolant fluid and are therefore not replaceable.

Milling is characterized by a varying undeformed chip thickness and interrupted tooth engagement along the tool rotation. This causes a periodic oscillation of the process forces due to the non-uniform crosssection of the uncut chip. For an ideally rigid four-fluted end mill and thin-walled workpiece, as illustrated in Fig. 5a, the geometric engagement condition is characterized by the depth of cut a_p and the width of cut a_e. From an isometric view, the teeth pass from left to right through the contact zone, removing chips from the workpiece along the tooth contact lines. The interaction between the tool and workpiece generates process forces at these contact lines. These process forces generate a resulting total bending moment M_b, which is measured by the strain gauges located within the tool holder. As the tool rotates, the magnitude of the bending moment M_b varies due to the changing number of simultaneously engaged teeth and the non-uniform cross-section of the undeformed chip per tooth, as shown on the right in Fig. 5a. Another contributing factor is the changing lever arm, as the tooth contact lines move upward within the engagement zone toward the measurement point.

In Fig. 5b, the compliance of the workpiece is taken into account. When machining compliant near-net-shape components, the compliance of the workpiece is often significantly higher than that of the tool xand machine combined. Therefore, geometric errors arise primarily from workpiece deflection. To limit the complexity of the proposed method, the tool and the machine are assumed to be ideally rigid and not subject to deformation. At each point along the tooth contact lines, the discretized generated process force can be decomposed into vector components. The force component acting perpendicular to the workpiece surface, integrated and summed over all tooth contact lines, is defined as the feed normal force F_{fN}, which causes the workpiece to deflect away from the tool. This reduces the effective width of cut $a_{e,\mathrm{eff}}$ which is no longer constant along the axial length of the end mill as a result of workpiece deflection. In the isometric view, the reduced size of the contact zone and the contact lines of the teeth can be observed. As a result, the time instances at which the teeth enter and exit the contact zone change. This alters the pattern of the resultant bending load in a characteristic way. If the correlation between these changes in the bending moment pattern and the deflection state of the workpiece is known, the toolpath can be adapted to compensate for the deflection.

In Fig. 5c, the tool's rotational axis is inclined by the tilt angle θ_t about the tool center point (TCP) towards the workpiece in order to reduce the geometric error. Additionally, the deflection at the height

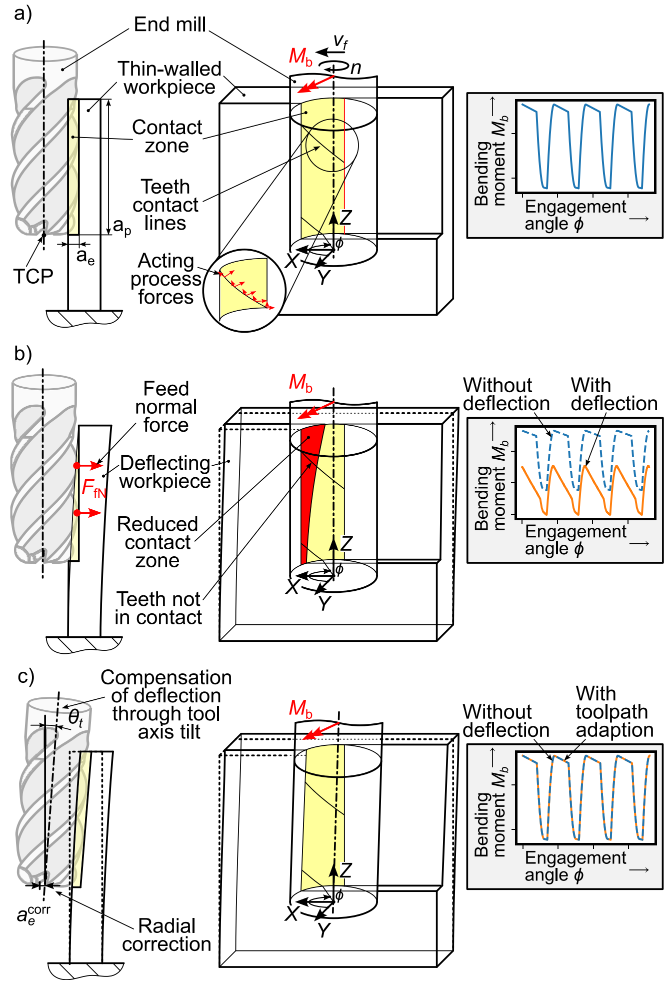

Fig. 5. Principle of predicting workpiece deflection by monitoring variations in the resultant bending moment pattern: (a) Ideal case without deformation; (b) Workpiece deflection due to feed normal force; (c) Compensation by tilting tool axis.

of the TCP is compensated with a width of cut correction a_e^{corr}. In the cross-sectional and isometric view, it can be seen that the width of cut a_e is now approximately constant along the depth of cut a_p of the end mill. As a result, the bending moment pattern becomes similar to that in Fig. 5a, where no deflection occurs, due to the matched size of the contact zone and length of the teeth contact lines.

2.2. Modeling the resultant bending moment pattern

A model was developed to analyze the influence of workpiece deflection on the bending moment pattern. This section introduces the fundamental equations and the assumptions used in modeling the cutting process.

2.2.1. Model description

Fig. 6a shows an isometric view of the interaction between an end mill of diameter d and a thin-walled workpiece during circumferential milling. As the tool rotates with spindle speed n and advances with feed velocity v_f parallel to the workpiece, chips are removed in the contact zone along the tooth contact lines, highlighted in yellow. To prevent the entire cutting edge from engaging simultaneously, which can induce vibrations and to improve chip evacuation, the tool teeth are inclined by the helix angle λ. The contact zone is geometrically defined by the depth of cut a_p and the width of cut a_e of the end mill. Referenced tool

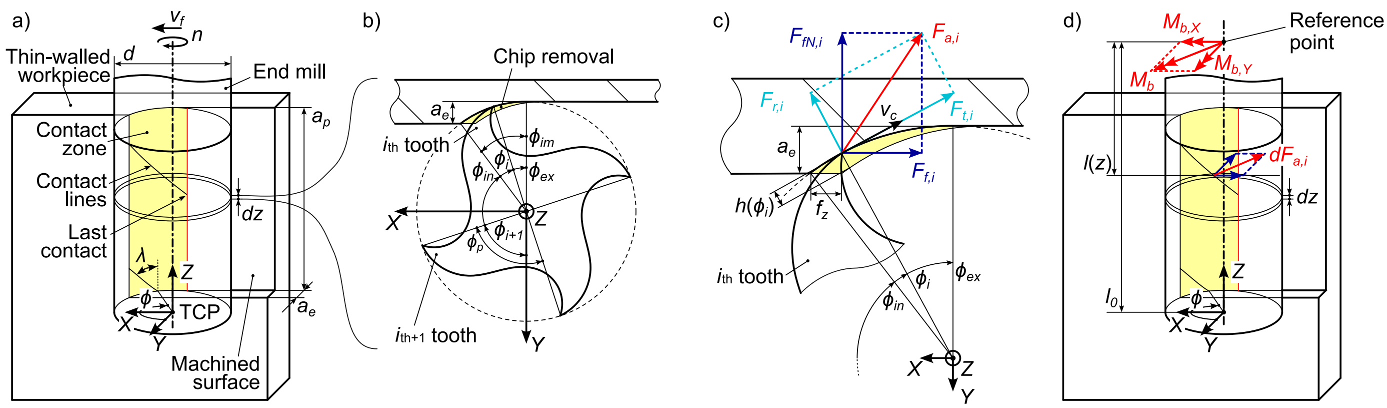

Fig. 6. Modeling of the bending moment in circumferential milling: (a) Isometric view of the tool–workpiece interaction; (b) Cross-sectional view with angle notation; (c) View of an engaging tooth and the resulting process forces; (d) Illustration of the resulting bending moment.

coordinate system is defined with its origin at the TCP, located at the bottom center of the tool. The X-axis points in the direction of the feed velocity v_f, while the Z-axis is aligned with the tool's rotational axis. The tool's rotation angle is denoted as the engagement angle ϕ.

In Fig. 6b, a discretized cross-section of the tool–workpiece interaction is shown. The tool teeth are numbered in the order in which they pass through the positive Y-axis, ranging from $i = 1, \dots, z$, with z denoting the total number of teeth. At an engagement angle of $\phi = 0°$, the first tooth is located at the height of the TCP ($Z = 0$) on the positive Y-axis. Unless otherwise noted, all angles are specified relative to the positive Y-axis. in a discretized cross-section the chip removal begins when a tooth passes the entry angle ϕ_{in} and ends when it passes the exit angle ϕ_{ex}, thereby defining the immersion angle ϕ_{im}:

$$\phi_{in} = \arccos\left(\frac{2 \cdot a_e}{d} - 1\right), \tag{1}$$

$$\phi_{ex} = \pi, \tag{2}$$

$$\phi_{im} = \phi_{ex} - \phi_{in}. \tag{3}$$

In down milling, where the tooth engages the material in the same direction as the workpiece moves relative to the tool, the entry angle ϕ_{in} depends on the width of cut a_e and the end mill diameter d. The exit angle ϕ_{ex}, on the other hand, is independent of the cutting conditions and tool geometry. For any point on the ith tooth at an axial position Z the engagement angle ϕ_i is given by:

$$\phi_i(\phi, Z) = \phi - (i-1) \cdot \phi_p - \phi_{lag}(Z). \tag{4}$$

The angular distance between two adjacent teeth, referred to as the pitch angle ϕ_p and the angular delay ϕ_{lag} - which describes how a point on the cutting edge at axial position Z is delayed relative to the bottom tip of the tooth due to the helix angle λ - can be calculated as:

$$\phi_p = \frac{2 \cdot \pi}{z}, \tag{5}$$

$$\phi_{lag}(Z) = \frac{2\tan(\lambda)}{d} Z. \tag{6}$$

The cross-sectional view in Fig. 6c illustrates the variable undeformed chip thickness $h(\phi_i)$ as tooth i enters the contact zone with cutting speed v_c at the entry angle ϕ_{in}. For down milling, when the width of cut a_e is smaller than the end mill radius $d/2$, the undeformed chip thickness $h(\phi_i)$ continuously decreases as the engagement angle ϕ increases, resulting in a comma-shaped chip being removed from the workpiece. If the cutting speed v_c is relatively high compared to the feed velocity v_f, the undeformed chip thickness $h(\phi_i)$ can be described as

$$h(\phi_i) = f_z \sin(\phi_i(Z)), \tag{7}$$

where f_z is the feed per tooth. For modeling the process forces, the cutting force model of Kienzle is applied [18]. It is based on the observation of an approximately proportional relationship between the tangential force F_t and the uncut chip cross-section A:

$$F_t \propto A \tag{8}$$

For circumferential milling with a non-constant uncut chip cross-section $A(\phi)$, a differential formulation is used. Therefore the tangential force $F_{t,i}$ is expressed for discretized disk elements along the axial direction and for each tooth i, based on the local undeformed chip thickness $h(\phi_i)$, as

$$dF_{c,i} = k_c \cdot h(\phi_i), \tag{9}$$

where k_c is the specific cutting force coefficient. Deviating from the simplified proportionality assumption, experience shows that the specific cutting coefficient k_c is not constant. It depends on factors such as material properties, cutting speed v_c, cutting edge geometry and undeformed chip thickness h [18]. However, this model assumes that the specific cutting coefficient k_c remains constant despite variations in undeformed chip thickness h, in line with the approach of Choi et al. [17]. It is therefore introduced as a simplification to reduce model complexity and to focus on the qualitative influence of geometric process parameters on the signal characteristics. This assumption is further justified by the fact that changes in the specific cutting coefficient primarily affect the magnitude of the cutting forces, while the characteristic pattern of the signal used for feature extraction is mainly governed by the geometric engagement conditions. Perpendicular to the tangential force $F_{t,i}$ acts the radial force $F_{r,i}$, which together span the active force $F_{a,i}$ in the X-Y plane. In this paper the ratio between the tangential force $F_{t,i}$ and the radial force $dF_{r,i}$ is assumed to be constant. The component of the active force $F_{a,i}$ acting perpendicular to the plane of the thin-walled workpiece is referred to as the feed normal force $F_{fN,i}$. It acts in the direction of maximum workpiece compliance and causes its deflection.

Fig. 6d illustrates how, in this model, the differential active force $dF_{a,i}$ of a single discretized disk element contributes to the bending moment M_b at the reference point located at a distance l_0 from the TCP. First, the differential active force $dF_{a,i}$ is decomposed into its X–Y-components in the tool coordinate system. Then, its force components are multiplied by the lever arm $l(Z)$ to the reference point to obtain the corresponding differential bending moments $dM_{b,X}$ and $dM_{b,Y}$. Finally, by integrating along the rotational axis Z and summing over the number of teeth z, the bending moments $M_{b,X}$ and $M_{b,Y}$ are obtained:

$$M_{b,q} = \sum_{i=1}^{z} \int_{Z_1}^{Z_2} l(Z) \cdot dF_{q,i}\, dz, \quad q \in \{X, Y\}. \tag{10}$$

The lever arm $l(Z)$ is calculated as

$$l(Z) = l_0 - Z. \tag{11}$$

With the bending moments $M_{b,X}$ and $M_{b,Y}$ around the X- and Y-axes, respectively, the resulting bending moment M_b is calculated as:

$$M_b = \sqrt{M_{b,X}^2 + M_{b,Y}^2}. \tag{12}$$

To account for the deflection in this model, Euler–Bernoulli beam theory is applied by representing the thin-walled workpiece as a beam with second moment of area I and elastic modulus E. The Euler–Bernoulli equation, which describes the relationship between the beam's deflection w and the applied load q, is given by:

$$\frac{d^2}{dx^2}\left(EI\frac{d^2 w}{dx^2}\right) = q. \tag{13}$$

The main purpose of using the Euler–Bernoulli formulation in this model is to capture the approximate qualitative shape of the bending-moment signal for a deflecting workpiece with a non-constant effective width of cut along the tool axis. This reduced-order formulation is used to avoid excessive FEM simulations and to provide physical insight into how constant variations in a_p, a_e and non-constant deflection-induced changes in $a_{e,\mathrm{eff}}$ influence the bending-moment signal. Although deviations from a full FEM-based solution are expected, the aim is to investigate whether the characteristic features of the simulated bending moment signal can be compared with those observed in the experimental measurements. Since the deflection of the beam results in a change in the cutting conditions, particularly a change in the width of cut a_e, which again results in a change in process forces, an iterative solution was applied until equilibrium was reached.

2.2.2. Model postprocessing

In Fig. 7, the model is evaluated for an ideally rigid workpiece with no deflection using the defined input parameters, illustrating the post-processing of the model output. Fig. 7a depicts the unrolled tool–workpiece contact zone with the colored contact lines of the individual teeth traveling from left to right. Cases i–iv correspond to the instances in time when tooth 1 passes through the corners of the contact zone. Since these instances are essential for the bending moment pattern M_b, in this paper they are labeled A–D in counterclockwise order.

In Fig. 7b, the modeled toothwise bending moment $M_{b,i}$ is plotted over one tool rotation, with the instances in time marked at which tooth 1 passes through A–D. As tooth i enters the contact zone at A, corresponding to the entry angle ϕ_{in} (case i), the toothwise bending moment $M_{b,i}$ begins to rise, referred to as the *rising point*. Maximum toothwise bending moment $M_{b,i}$ is reached when the tooth arrives at B, the exit angle ϕ_{ex} and is fully engaged in the contact zone (case ii). With further increase of the engagement angle ϕ, the tooth moves upward within the contact zone. Although the cross-section of the undeformed chip does not change, the toothwise bending moment $M_{b,i}$ is reducing due to the shortening lever arm l. As the tooth's contact line reaches C at the upper boundary of the contact zone (case iii), the toothwise bending moment $M_{b,i}$ starts to decrease. This point in time is referred to as the *falling point*. The tooth disengages completely from the workpiece once D is passed (case iv).

At certain engagement angles ϕ, multiple teeth are engaged simultaneously. In these cases, the toothwise bending moment $M_{b,i}$ add up to the total bending moment M_b, as shown in Fig. 7c. Since the signal pattern repeats at intervals of the pitch angle ϕ_p (Eq. (5)), the model output is restricted to a single period. Within this period the curve falls due to the disengagement of the previous tooth (tooth 4). These points are marked as C_4 and D_4. As a post-processing step, the signal is normalized using a *min–max scaler* to the range 0-1, in order to better illustrate and compare the signal patterns, as shown in Fig. 7d [19].

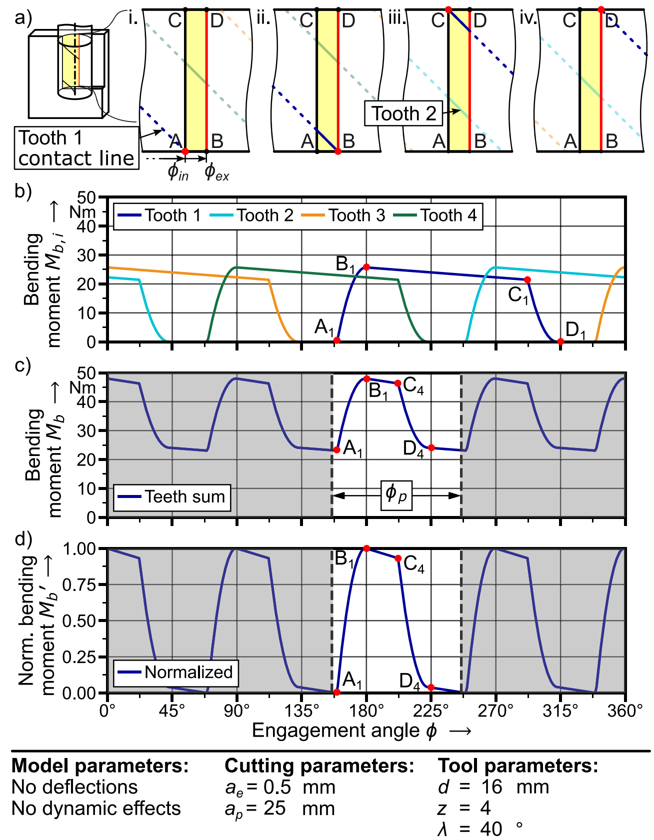

Fig. 7. Postprocessing to the signal of the modeled bending moment M_b: (a) Unrolled tool–workpiece contact zone; (b) Modeled toothwise bending moment $M_{b,i}$; (c) Modeled total bending moment M_b; (d) Normalized total bending moment.

2.3. Experimental validation

This section summarizes the milling tests on thin-walled workpieces, in which an integrated sensor was used to collect in-process data for validating the developed bending moment model.

2.3.1. Experimental setup

The milling tests were carried out on a 5-axis gantry machining center *FOOKE ENDURA 711 Linear*, shown in Fig. 8a. The reference process considered is based on the manufacturing of lightweight structural components in the aerospace industry made from titanium alloy (Ti-6Al-4V). As a reference analogy part representing a stiffening rib, titanium sheets with a thickness of $t_r = 2.5\,\mathrm{mm}$ were used, clamped at the bottom and one side in a clamping device, as shown in Fig. 8b and Fig. 8c. Since the compliance and deflection response of the workpiece strongly depend on the workpiece geometry and the fixture boundary conditions, different configurations result in different bending moment patterns. Therefore, this setup was chosen such that the local compliance and thus the deflection of the workpiece varies during machining, enabling the collection of a wide range of data for model validation. The workpiece has a length of $l_r = 150\,\mathrm{mm}$ and a height of $h_r = 55\,\mathrm{mm}$, measured relative to the bottom and side clamping. Highlighted in yellow, the surface to be machined was measured using a machine tool–integrated measuring probe, the *Renishaw RMP60*, which has a repeatability of $1\,\mu\mathrm{m}$. It was verified that the surface to be machined was within a tolerance of $\pm 20\,\mu\mathrm{m}$ relative to an ideal reference plane.

The machining operation was carried out using an unworn, four-flute solid carbide finishing end mill with a diameter of $d = 16\,\mathrm{mm}$, helix angle $\lambda = 40°$ and constant pitch angle $\phi_p = 90°$. It consisted of a circular tool entry with a radius of $r_{\mathrm{in}} = 3\,\mathrm{mm}$ at half the feed velocity v_f to reduce tool wear by minimizing tool exit failure [20]. This was followed by parallel advancement at a constant feed velocity v_f over a feed travel of $l_f = 120\,\mathrm{mm}$, from the fixed end to the free end of the thin-walled workpiece. The nominal depth of cut a_p and width of cut a_e were kept constant for each individual test run.

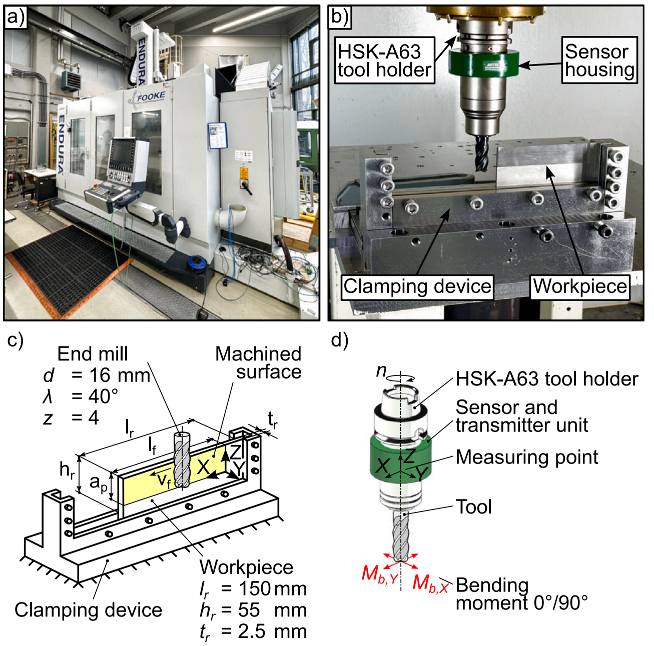

Fig. 8. Experimental setup: (a) FOOKE ENDURA 711 Linear 5-axis gantry machining center; (b) Clamping device and workpiece; (c) Schematic representation of clamping device and workpiece; (d) Schematic representation of rotating sensor system.

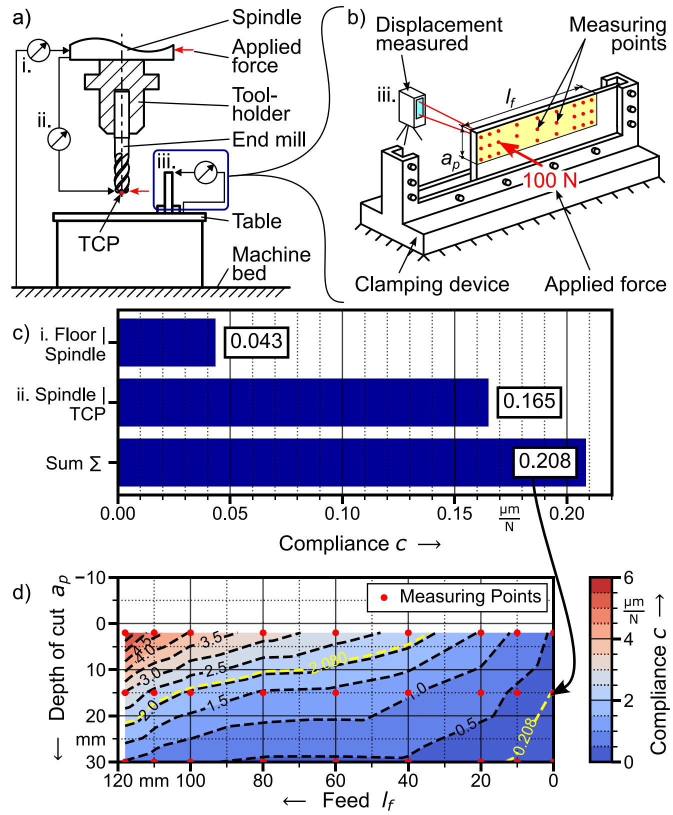

Fig. 9. Analysis of static compliance: (a) Measurement points on the machine/tool; (b) Measurement points on the workpiece; (c) Compliance results of the machine/tool; (d) In-plane compliance results of the workpiece.

2.3.2. *Static compliance of experimental setup*

In the derived bending moment model, the simplification was made that only the workpiece deflects, while the tool and the machine are assumed to be ideally rigid. To validate this assumption, a static compliance analysis was conducted of all components in the load path. The test setup is visualized in Fig. 9a. The handheld force measuring device *PCE - FG500* was used to apply point loads of $F = 100\,\mathrm{N}$ in the directions shown. Along the direction of the applied force the laser-based displacement sensor *Micro-Epsilon ILD2300-10* was used to measure deflection. For the thin-walled workpiece, multiple measurement points were recorded on a grid across the machined surface, with finer spacing near the free and fixed ends where larger gradients were expected, as shown in Fig. 9b.

The measured compliances are shown in Fig. 9c and d, for both the machine components and the machined surface of the workpiece. At the free end (top-left), the workpiece exhibited a compliance of approximately $5\,\mathrm{\mu m\,N^{-1}}$, which is around 20 times higher than the combined compliance of all other components in the load path, which amounts to $0.2\,\mathrm{\mu m\,N^{-1}}$. However, near the fixed end, the workpiece shows a comparable amount of compliance and the deflection of the end mill and machine should be taken into account. In this region, deviations between the model and the experimental data may occur, as the tool is assumed to be ideally rigid in the model.

2.3.3. *Process parameters*

Cutting parameters are summarized in Table 1. For each parameter combination, two milling experiments were performed to evaluate repeatability.

2.3.4. *Data acquisition and signal post-processing*

Bending moment. The used sensor records the bending moment around the X-direction $M_{b,X}$ and in the Y-direction $M_{b,Y}$, as illustrated in Fig. 8d, corresponding to the sensor's internal rotating coordinate system. From the two channels the overall bending moment M_b is obtained according to Eq. (12). Maximum bending moment is specified as $M_b^{\max} = 240\,\mathrm{N\,m}$ and maximum spindle speed $n^{\max} = 18.000\,1/\mathrm{min}$.

Table 1
Cutting parameters used in the milling experiments.

Parameter	Symbol	Value
Cutting speed	v_c	$35\,\mathrm{m\,min^{-1}}$, $50\,\mathrm{m\,min^{-1}}$
Spindle speed	n	696 1/min, 994 1/min
Feed per tooth	f_z	0.1 mm
Depth of cut	a_p	20 mm, 25 mm
Width of cut	a_e	0.5 mm
Repetitions	–	2

The sensitivity of the sensor system, derived from the measurement resolution and the maximum measurable bending moment, is approximately $\Delta M_b = 0.0073\,\mathrm{N\,m}$. The limited bandwidth of the wireless transmission restricts the sensor sampling rate to $f_s = 2000\,\mathrm{Hz}$. At a cutting speed of $v_c = 50\,\mathrm{m\,min^{-1}}$, corresponding to a spindle speed of $n = 994\,\mathrm{min^{-1}}$, this yields approximately 121 sample points per tool revolution.

Fig. 10a shows the measured bending moment M_b in full extent. The signal has been trimmed to the section of the linear toolpath, removing the tool entry sequence, as shown in Fig. 10b. To enable more precise signal processing in the following steps, the signal is artificially resampled to a higher sampling rate using the Fourier method [21]. The sampling frequency f_s is artificially increased to provide 360 sample points per tool rotation.

Due to runout errors caused by manufacturing limitations, individual teeth may have a slightly larger or smaller diameter than the nominal tool diameter d and thus remove more or less material than adjacent teeth. To account for this, a periodic averaging method is applied following the approach of Choi et al. [17], enabling a better comparison with the model. This method is based on the concept that the bending moment M_b signal repeats over the pitch angle period ϕ_p

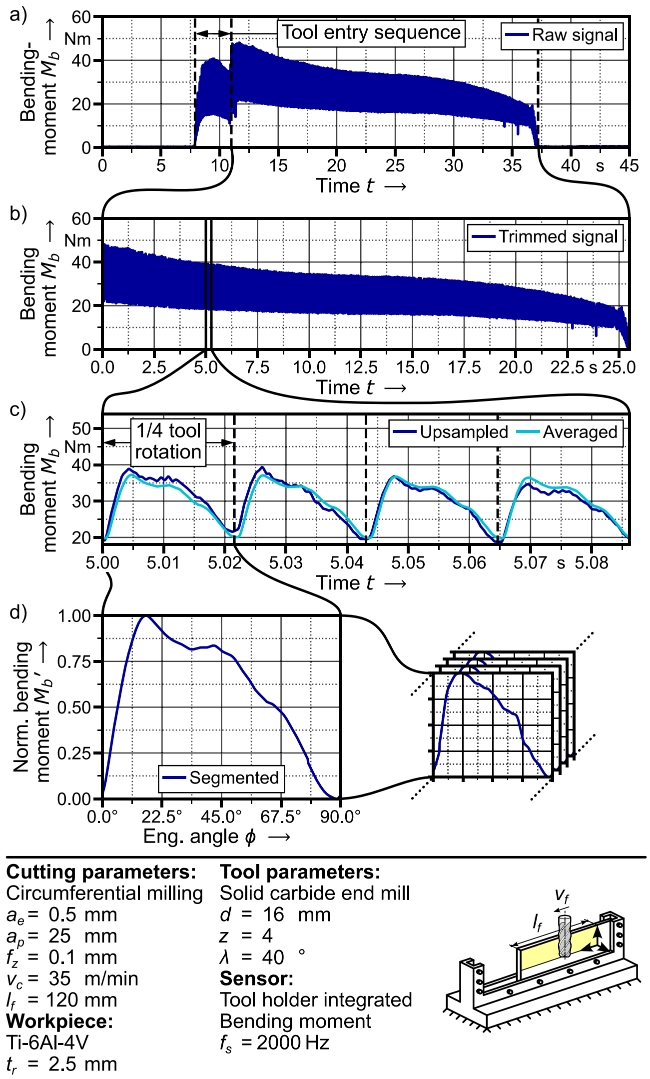

Fig. 10. Measured bending moment M_b: (a) Raw signal; (b) Extracted relevant signal; (c) Signal for a single tool rotation; (d) Segmented signal for a single tooth passage.

of the teeth. Knowing the tooth passing period T_{tp}, which is calculated as

$$T_{tp} = \frac{60}{n \cdot z}, \tag{14}$$

the signal $x(t)$ can be processed using

$$y(t) = \frac{1}{N_s} \sum_{j=1}^{N_s} x(t + (j-1) \cdot T_{tp}), \tag{15}$$

where N_s denotes the number of periods used for averaging. However, the application of periodic averaging limits the method to cutters with a constant pitch angle ϕ_p and helix angle λ. Otherwise, the bending moment M_b signal does not repeat over a pitch period, since the cutting volume varies for each tooth. To enable the use of such cutters, the model described in Section 2.2 would need to be extended to account for non-constant pitch angles ϕ_p and helix angles λ. After modeling the bending moment M_b, periodic averaging could then be applied to the modeled signal. The upsampled signal and averaged signal is plotted in Fig. 10c for one tool rotation.

In the final step, the signal is segmented into intervals of the tooth passing period T_{tp}, which corresponds to the pitch angle $\phi_p = 90°$ (Eq. (5)), shown in Fig. 10d. The values within each segment are

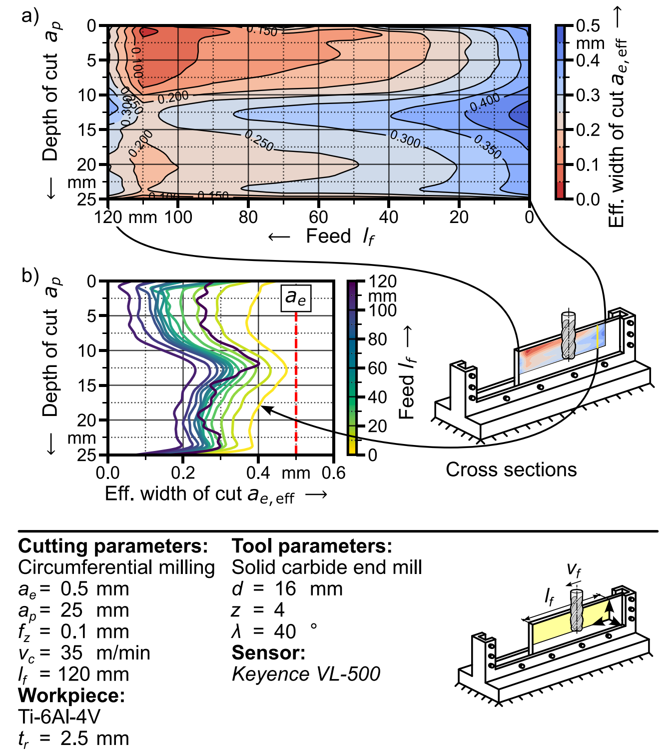

Fig. 11. Measured effective width of cut a_e: (a) Overall machined surface; (b) Cross-sectional trends of the machined surface.

then normalized to the range $[0, 1]$ using a *Min–Max-Scaler* to facilitate comparison and to highlight small variations in the pattern caused by workpiece deflection [19].

Workpiece deflection. To quantify the workpiece deflection during machining resulting in the geometric error, the workpiece thickness was measured before and after machining using the optical 3D coordinate measuring system *Keyence VL-500*. Fig. 11a shows the calculated effective width of cut $a_{e,\mathrm{eff}}$ of the machined surface. In Fig. 11b, cross-sections taken every 10 mm in the feed direction are plotted, illustrating the wavy surface pattern caused by an alternating number of simultaneously engaged teeth. This effect is further explained in detail by Wimmer et al. [22].

3. Results and discussion

3.1. Model evaluation under varying engagement conditions

In this section, the model from Section 2.2 is evaluated and the effects of variations in geometric engagement conditions on the bending moment M_b are examined.

3.1.1. Variations in width of cut a_e

To illustrate the influence of variations in the width of cut a_e while keeping all other process parameters constant, Fig. 12 presents the evaluated model for three different widths of cut ranging from $a_e = 0.1 - 0.5$ mm. For better comparison, the curves are plotted in the same figure, with transparency levels varying according to the width of cut a_e, as indicated in the figure color bar. As described in Fig. 7, the red dots denote the moments in time when the corresponding tooth contact line passes the corners A–D of the contact zone. Illustrated in Fig. 12a, a decrease in width of cut a_e leads to a smaller immersion angle ϕ_{im} (Eq. (3)) and the contact zone is getting narrower. As the width of cut a_e decreases, the timing of the tooth passing points A and C is delayed.

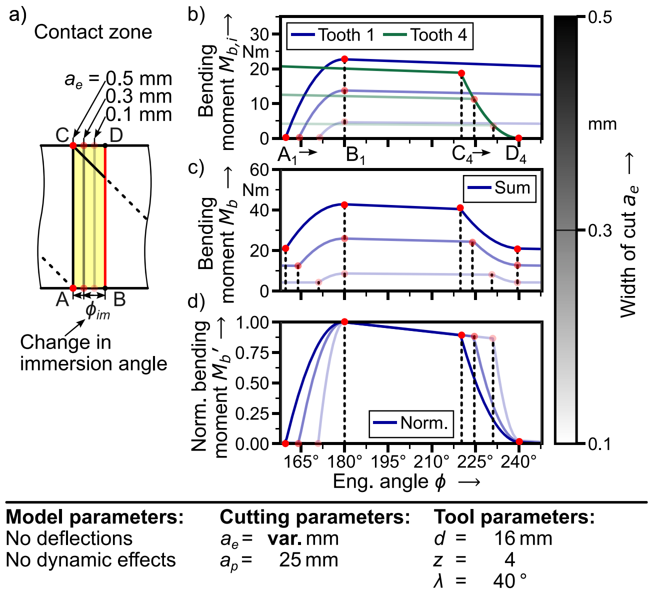

Fig. 12. Effect of variations in width of cut a_e on: (a) the geometry of the contact zone; (b) the toothwise bending moment $M_{b,i}$; (c) the total bending moment M_b; and (d) the normalized bending moment M_b' pattern.

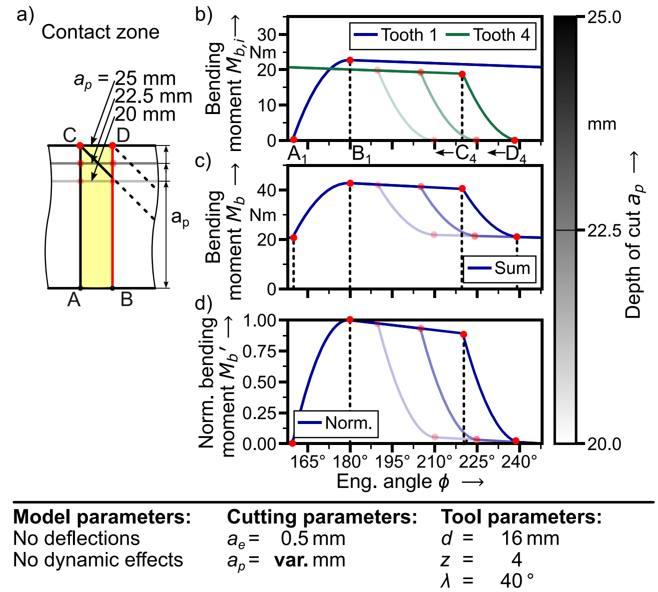

Fig. 13. Effect of variations in depth of cut a_p on: (a) the geometry of the contact zone; (b) the toothwise bending moment $M_{b,i}$; (c) the total bending moment M_b; and (d) the normalized bending moment M_b' pattern.

Consequently, as seen in Fig. 12b, the curve rises at a later point in time after passing A. At the same time, because a smaller portion of the cutting edge is engaged simultaneously, the maximum magnitude of the toothwise bending moment $M_{b,i}$ is reduced as the cutting edge hits corner B in the contact zone. This can also be observed in Fig. 12c for the total bending moment M_b. Nevertheless, the point in time at which the maximum occurs remains unchanged. When the cutting edge exits the contact zone at its top, the point in time passing edge C shifts backward for a decreasing width of cut a_e. This results in Fig. 12b–c in the curve falling at a higher engagement angle ϕ.

To summarize, the following characteristics of the normalized bending moment M_b' can be observed in Fig. 12d as the width of cut a_e decreases:

i. The rising point (A) is delayed, resulting in an steeper initial slope of the curve.
ii. The falling point (C) is delayed, leading to a steeper decline of the curve afterward.
iii. The maximum (B) as well as the point in time at which the previous tooth disengages completely (D) is not affected.

3.1.2. Variations in depth of cut a_p

The effect of varying the depth of cut a_p on the bending moment M_b is illustrated in Fig. 13. When the depth of cut a_p is reduced, the height of the contact zone decreases, as shown in Fig. 13a. While A and B remain geometrically unaffected, C and D shift downward as the depth of cut a_p decreases. For the toothwise bending moment $M_{b,i}$ signal, plotted in Fig. 13b, this corresponds to the falling point occurring earlier in time (C), as well as an earlier moment of disengagement of the tooth from the workpiece (D). This is also visible for the toothwise summed bending moment M_b in Fig. 13c. Fig. 13d illustrates the corresponding changes in the normalized bending moment M_b' resulting from variations in the depth of cut a_p.

If the depth of cut a_p decreases:

i. The rising point (A) and the maximum (B) are not affected.
ii. The falling point (C) occurs earlier.
iii. The point at which the previous tooth disengages completely (D) occurs earlier.

3.1.3. Variations in deflection of workpiece

In the previous sections, the workpiece was assumed to be ideally stiff. In this section and Fig. 14, the effect of workpiece deflection on the bending moment M_b pattern is examined for a non-ideally stiff workpiece, modeled with Euler–Bernoulli beam theory (Eq. (13)). The width of the beam and therefore the second moment of area I, was altered to observe three different deflection states: No deflection as a comparison; Minor deflection, so the width of cut a_e is halved at the top end of the contact zone; Major deflection, so the width of cut a_e at the top end is zero. In Fig. 14a, the geometry of the tool–workpiece contact zone is illustrated for the three different workpiece deflection states. For a deflected workpiece, it can be observed that the immersion angle ϕ_{im} narrows as the teeth approach the upper free end of the workpiece. This occurs because the thin-walled workpiece is clamped at the bottom, causing the upper free end to deflect more than the region near the fixed support. The effect becomes increasingly pronounced as the workpiece deflection grows. As illustrated in Fig. 14a, corners A and C are geometrically altered, whereas B and D remain unaffected for the deflecting workpiece.

Fig. 14b illustrates the effect on the toothwise bending moment $M_{b,i}$. Since the contact zone narrows slightly at the bottom, the rising point is slightly delayed as the teeth pass point A. In contrast, because the contact zone becomes significantly narrower at the free (upper) end of the workpiece, the teeth pass point C later compared to a non-deflecting workpiece. The engagement angles ϕ at which the teeth pass points B and D remain unchanged.

Figs. 14c–e illustrate the toothwise summed bending moment M_b, the normalized bending moment M_b' and its first derivative, respectively. The derivative in Fig. 14e clearly indicates the moment when the tooth crosses C, causing the curve to decline.

In summary, if the workpiece deflection increases:

i. The rising point (A) is delayed marginally.
ii. The maximum (B) is not affected in terms of timing.
iii. The falling point (C) is delayed.
iv. The point at which the previous tooth disengages completely (D) is not affected.

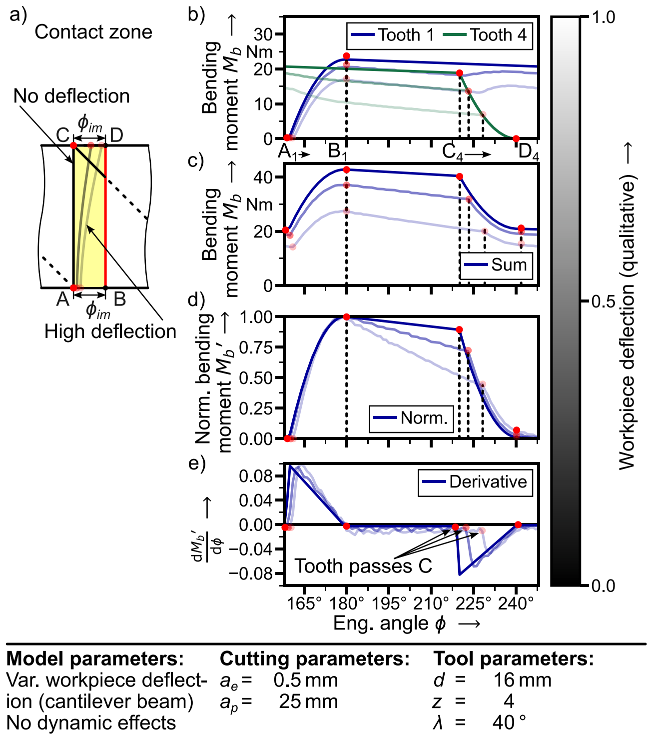

Fig. 14. Effect of variations in workpiece deflection on: (a) the geometry of the contact zone; (b) the toothwise bending moment $M_{b,i}$; (c) the total bending moment M_b; (d) the normalized bending moment M_b pattern; and (e) the first derivative of the normalized bending moment M_b'.

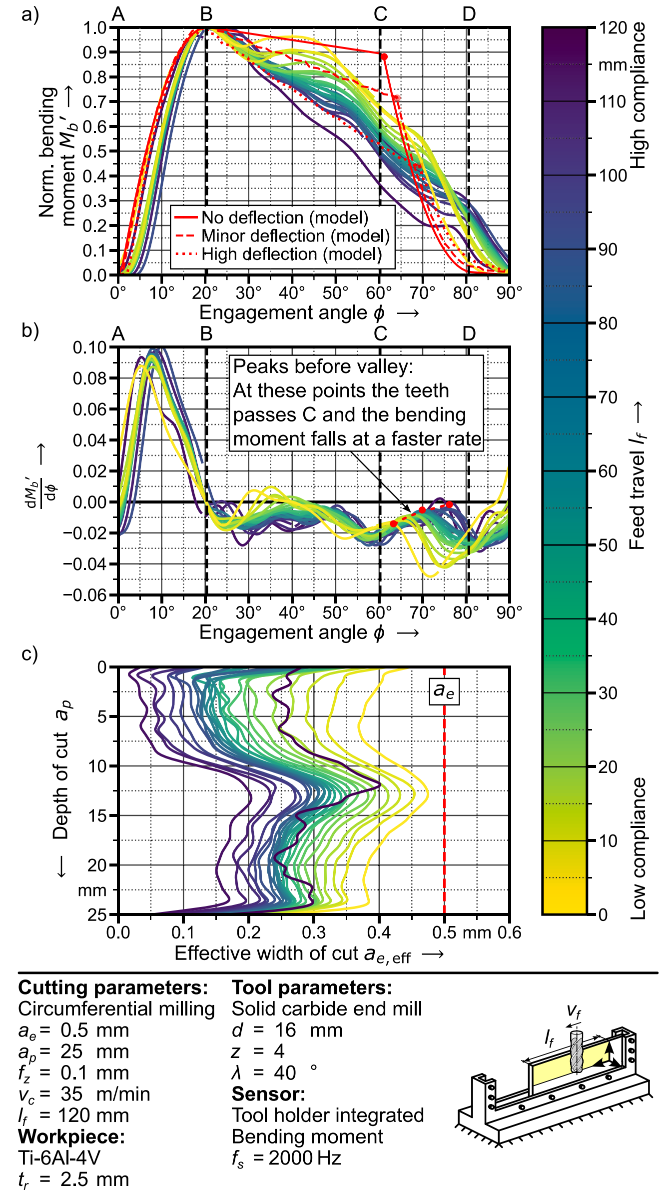

Fig. 15. Processed and segmented bending moment signal: (a) Segmented and normalized signal with the plotted model for three different deflection states; (b) First derivative of the segmented and normalized signal. (c) Measured effective width of cut $a_{e,\mathrm{eff}}$.

3.2. Comparison of in-process data and model

In this section, the post-processed in-process data from Section 2.3 are compared with the derived model. In Fig. 15a one segment of the signal every 5 mm of feed travel l_f is plotted to visualize the trend of the pattern as the deflection of the workpiece increases. In addition, the model-data is plotted in red for three different workpiece deflection states, as introduced in Fig. 14. Fig. 15b shows the first derivative of each segment. In Fig. 15c the measured corresponding effective width of cut $a_{e,\mathrm{eff}}$ is plotted. The following findings observed in the model with deflection modeled using Euler–Bernoulli beam theory can also be identified in the in-process data:

i. *The rising point (A) is delayed marginally*: Since the workpiece deflects more at the top end and only little at the bottom end, as this section is closer to the bottom fixed end, the immersion angle ϕ_{im} decreases marginally. Therefore the time period between the tooth passes A and B decreases marginally.

ii. *The maximum (B) is not affected in terms of timing*: The exit angle ϕ_{ex} does not change under varying engagement conditions (Eq. (2)). In addition, this point has been used to align the segment.

iii. *The falling point (C) is delayed*: This can be better observed in Fig. 15b, where the first derivative of the normalized bending moment M_b' segments is plotted. Here, the peak preceding the valley between points C and D is delayed as the tool approaches the upper free end and the workpiece deflects further. This could be an indication of the decreasing immersion angle ϕ_{im} at the top end of the workpiece.

iv. *The point at which the previous tooth disengages completely (D) is not affected*: At this point, there is a deviation between the data and the model. In Fig. 14e, it can be seen that at point D the curves return to a steady, constant state after the tooth passes D. However, in Fig. 15b, at D the curves have not returned to a steady state but are still oscillating. An explanation for this discrepancy cannot be explained by a dynamic effect such as forced vibrations of the workpiece during elastic spring-back when the tooth exits the workpiece. An experimental modal analysis was conducted for the workpiece, resulting in a first eigenfrequency of $f_1 = 2700$ Hz, which is more than 50 times higher than the tooth passing frequency of $f_{tp} = 46$ Hz for the experiments with a cutting speed of $v_c = 35\,\mathrm{m\,min^{-1}}$ and $f_{tp} = 66$ Hz for the experiments with a cutting speed of $v_c = 50\,\mathrm{m\,min^{-1}}$. Nevertheless, the observed discrepancy is not attributed to random vibrations, since all curves in Fig. 15b consistently exhibit a steady oscillatory behavior at point D over the feed travel l_f.

In addition, a deviation between the model and the in-process data can be expected since the machine and tool are not ideally stiff as assumed in the model. This is particularly the case in the feed travel l_f range of 0 – 20 mm, as shown by the compliance analysis of the workpiece (Fig. 9d), since in that range the workpiece is as compliant as the machine and tool combined.

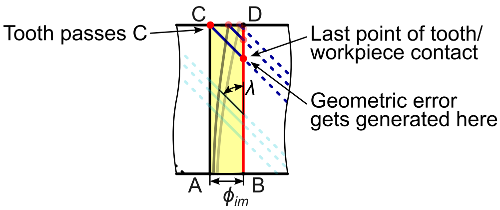

Fig. 16. The point of surface generation is shifted downward due to the tool helix angle λ.

3.3. Predicting workpiece deflection from the bending moment pattern

For the previously mentioned correlation, the in-process bending moment signal is used to predict the effective width of cut $a_{e,\mathrm{eff}}$ at the upper free end of the workpiece solely from the pattern of the signal. Therefore, the peak before the valley is determined for each segment. This is done by taking the second derivative and searching for a negative zero crossing of the curve. Since D should not be affected when neglecting dynamic effects, the immersion angle ϕ_{im} between these adjusting points is determined. With the immersion angle ϕ_{im} and the rearranged Eq. (3), the effective width of cut $a_{e,\mathrm{eff}}$ at the upper free end of the workpiece can be calculated. Due to the helix angle λ, the surface is not generated at the same axial height of the tool when the tooth passes C. This is visualized in Fig. 16. When passing C of the contact zone, the workpiece surface is created at the bottom end of the engaged tooth. At this point in time, the current workpiece deflection is transferred to a geometric error at the point of the last tooth/workpiece contact.

In Fig. 17a and b, the predicted effective width of cut $a_{e,\mathrm{eff}}$ at the upper free end of the workpiece is plotted against the measured width of cut for two different cutting speeds v_c. The predicted effective width of cut $a_{e,\mathrm{eff}}$ is obtained by evaluating the in-process bending moment data, while the effective width of cut $a_{e,\mathrm{eff}}$ from the milling experiments was obtained from the 3D coordinate measuring scan of the workpiece. Due to signal loss some datapoints are missing. The deviation from the measured to the predicted width of cut $a_{e,\mathrm{eff}}$ is calculated for these two experiments as the root-mean-square deviation (RMS), which is 0.053 mm and 0.076 mm, respectively. At a cutting speed of $v_c = 35\,\mathrm{m\,min^{-1}}$, 72% of the samples lie within a $\pm 50\,\mu\mathrm{m}$ tolerance band, while the maximum deviation between measurement and prediction reaches 480 µm. At $v_c = 50\,\mathrm{m\,min^{-1}}$, 62% of the samples fall within the $\pm 50\,\mu\mathrm{m}$ tolerance band, with a maximum deviation of 350 µm. Close to the free end of the workpiece at feedtravel $l_f = 120\,\mathrm{mm}$, a high deviation between prediction and measurement can be observed for both cutting speeds v_c. Near the edges of the workpiece (approximately $2-3\,\mathrm{mm}$), the data quality deteriorates due to the lack of a reliable measurement of the effective width of cut $a_{e,\mathrm{eff}}$ using the 3D coordinate measuring system *Keyence VL-500*. As measured and described in Section 2.3.2, close to the fixed end of the workpiece at a feed travel of $l_f = 0\,\mathrm{mm}$, the compliance of the workpiece reaches a level comparable to the combined compliance of the machine and the end mill. As a result, the effective width of cut $a_{e,\mathrm{eff}}$ is reduced not only due to workpiece deflection but also due to deflection of the machine and the tool. Nevertheless, the trend of the effective width of cut $a_{e,\mathrm{eff}}$ can still be predicted in this region. For the experiment at a cutting speed of $v_c = 50\,\mathrm{m\,min^{-1}}$ at a feed travel of $l_f = 0-10\,\mathrm{mm}$, a deviation between the predicted and measured effective width of cut $a_{e,\mathrm{eff}}$ can be observed.

Although the general trend of the effective width of cut $a_{e,\mathrm{eff}}$ at the upper free end of the workpiece along the feed travel l_f can be predicted by the proposed method for booth cutting speeds v_c, deviations are still present. One possible reason could be the limited sampling rate of $f_s = 2000\,\mathrm{Hz}$. At a cutting speed of $v_c = 50\,\mathrm{m\,min^{-1}}$, corresponding to a spindle speed of $n = 994\,\mathrm{min^{-1}}$, the engagement interval of a single

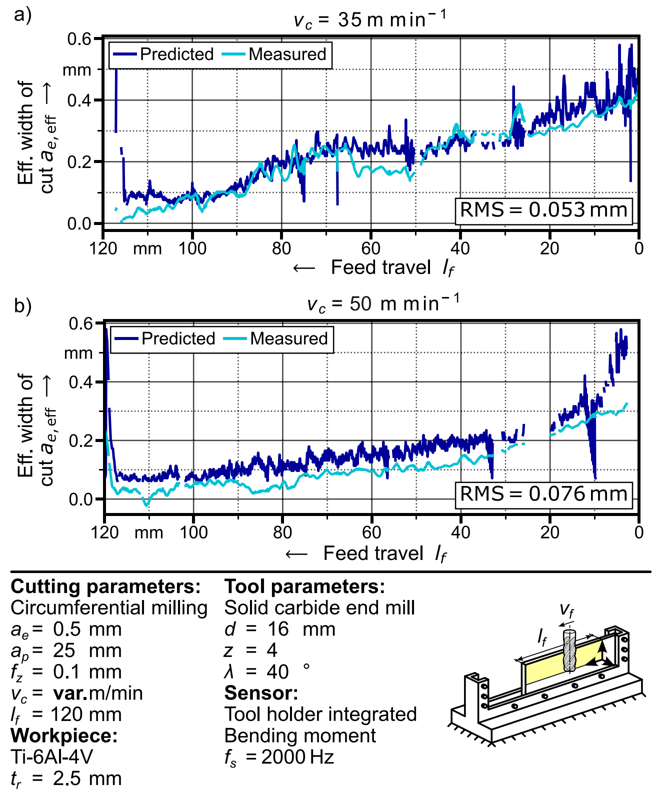

Fig. 17. Comparison of the predicted and measured effective width of cut $a_{e,\mathrm{eff}}$ at the upper free end of the workpiece.

tooth is only about 15 ms, during which approximately 30 samples are recorded by the sensor. As a result, small variations in the bending moment M_b signal may not be captured with sufficient resolution. This is, for example, the case for changes in the distance between points A and B when the width of cut a_e varies, as illustrated in Fig. 12. Another example is the distance between points C and D, which changes only slightly with increasing workpiece deflection, as shown in Fig. 14. It is therefore expected that the prediction accuracy can be improved by using a sensor with a higher sampling rate f_s.

4. Conclusion and outlook

4.1. Conclusion

The scope of this work was to predict the deflection of near-net-shape components, which are becoming increasingly relevant due to the growing use of additive manufacturing. For such components, conventional strategies such as waterline milling are often not applicable, as the geometry is already close to the final shape. The novelty of this approach was to analyze the correlation between the deflection state of the workpiece and the pattern of the measured bending moment M_b, in order to predict the workpiece deflection and derive the effective width of cut $a_{e,\mathrm{eff}}$. Therefore, a sensor system was used that employs strain gauges and wireless data communication, which is already available and applied in commercial applications. The bending moment M_b at a lever arm l_0 from the TCP was modeled for circumferential milling of thin-walled workpieces. It was investigated how variations in engagement conditions — specifically depth of cut a_p, width of cut a_e and workpiece deflection modeled as a bending cantilever beam — affect the pattern of the bending moment M_b.

While other methods often rely on the total magnitude of the cutting force — which is influenced by material properties, cutting edge geometry, tool wear, workpiece stiffness and other process parameters

— the advantage of the proposed method is that it depends solely on the tool geometry and the engagement conditions (width a_e and depth of cut a_p). It does not require a simulation of the local stiffness of either the workpiece or the tool. The results indicate that the bending moment pattern reveals distinct time points when the tool teeth cross the corners of the tool–workpiece contact zone. From these features in the signal, the deflection of the workpiece at the top end of the contact zone can be determined. The measured in-process data showed agreement with the derived simple bending moment model and the general trend of the effective width of cut $a_{e,\mathrm{eff}}$ at the upper free end of the workpiece along the feed travel l_f can be predicted by the proposed method. However, when compared to the typical wall thickness tolerance used in aircraft manufacturing of $\Delta t = \pm 0.05\,\mathrm{mm}$, only 62%–72% of the predictions lie within this range. A possible reason for improving the prediction accuracy is the use of a sensor system with a higher sampling rate f_s, which would allow better resolution of time-sensitive features in the bending-moment signal.

4.2. Outlook

The results have shown that the effective width of cut $a_{e,\mathrm{eff}}$ can still be predicted even when deflection of the tool and machine occurs simultaneously. This indicates that the proposed method is not strictly limited to workpiece-only deflection, but inherently captures the combined system response reflected in the bending-moment signal. Consequently, the approach has the potential to be generalized by explicitly accounting for both tool and workpiece compliance, which will be investigated in future work. Therefore, the bending-moment model needs to be adapted to also account for tool deflection.

The process parameters in this study were selected conservatively to ensure stable machining conditions. A key challenge in machining thin-walled workpieces is the occurrence of workpiece vibrations and chatter, which were not explicitly investigated in this work. Both chatter and forced vibrations can introduce additional high-frequency components into the bending-moment signal, potentially affecting the robustness of feature detection. Even though no chatter was observed in the experiments, it is expected that periodic averaging can reduce random measurement noise and improve feature robustness under stable cutting conditions. However, its effectiveness in the presence of chatter-related vibrations would require further investigation. Future work using the presented sensor system should therefore investigate the application of low-pass filtering to reduce the influence of high-frequency components. Alternatively, methods to identify chatter prior to signal evaluation could be developed, allowing for adaptive adjustment of the process parameters accordingly.

In future work, the proposed method is intended to be extended towards in-situ prediction of workpiece deflection in order to enable adaptive adjustment of the tool path during machining. The current signal processing and feature extraction pipeline mainly consists of lightweight operations such as signal segmentation, upsampling, periodic averaging and simple arithmetic feature computation. In addition, the low feed velocity v_f typically used when machining titanium components allows for comparatively relaxed timing constraints, with acceptable latencies on the order of approximately $0.1\,\mathrm{s}$. Therefore, the overall computational cost is expected to remain low and suitable for implementation on embedded hardware. In particular, deployment on a Raspberry Pi-class system is considered feasible, enabling near real-time evaluation of the bending-moment signal and subsequent process adaptation. Beyond this, future work will also consider the development of more advanced evaluation algorithms by incorporating robust machine learning methods, such as convolutional neural networks (CNNs), to analyze patterns in the bending-moment signal and improve the prediction of workpiece deflection.

The presented method is currently limited to predicting the dimensional error at the upper free end of the workpiece and does not yet capture the dimensional error along the tool axis. For adaptive toolpath correction, additional information is required to tilt the tool orientation relative to the deflecting workpiece. Future work should investigate whether the method can also be extended to predict the effective width of cut $a_{e,\mathrm{eff}}$ at the lower end of the depth of cut a_p. Initial evaluations in this paper indicate that this is generally feasible, but the results are not yet robust. One contributing factor is the limited sensor sampling rate of $f_s = 2000\,\mathrm{Hz}$, which restricts the resolution of small variations in the signal pattern. At the lower end of a_p, the workpiece deflection is smaller, resulting in reduced shifts of characteristic points (A and B) and therefore requiring a measurement system with higher temporal resolution. If the workpiece deflection at both the upper and lower ends of the depth of cut a_p can be determined, compensation could be achieved by appropriately tilting the tool. However, this approach requires that the resulting dimensional error varies approximately linearly along the depth of cut. Such approximately linear dimensional error can be achieved by an appropriate choice of the tool, as discussed in [22].

CRediT authorship contribution statement

Michel Kenneth Seiffert: Writing – original draft, Visualization, Software, Methodology. **Sebastian Junghans:** Writing – review & editing. **Lasse Evers:** Writing – review & editing, Validation. **Jan Hendrik Dege:** Writing – review & editing, Validation.

Declaration of competing interest

The authors declare that they have no known competing financial interests or personal relationships that could have appeared to influence the work reported in this paper.

References

[1] Azanaw GM. Thin-walled structures in structural engineering: A comprehensive review of design innovations, stability challenges, and sustainable frontiers. Am J Mater Synth Process 2025;10:18–26. http://dx.doi.org/10.11648/j.ajmsp.20251001.13.

[2] Schmitt T, Olives Juan S, Amouzgar K, Hanson L, Urenda Moris M. Optimizing energy efficiency and productivity in industrial manufacturing: A simulation-based optimization approach with knowledge discovery. J Manuf Syst 2025;82:748–65. http://dx.doi.org/10.1016/j.jmsy.2025.07.008.

[3] Bai H, Chen Y, Bai H, Liu M, Fan Y. Energy optimization and efficiency improvement model for enterprise production process based on deep learning under the background of carbon peak and carbon neutrality. Int J Comput Intell Syst 2025;18. http://dx.doi.org/10.1007/s44196-025-00901-9.

[4] Smith S, Schmitz T, Feldhausen T, Sealy M. Hybrid metal additive/subtractive machine tools and applications. CIRP Ann 2024;73(2):615–38. http://dx.doi.org/10.1016/j.cirp.2024.05.002.

[5] Lassila AA, Svensson D, Wang W, Andersson T. Numerical evaluation of cutting strategies for thin-walled parts. Sci Rep 2024;14(1):1459. http://dx.doi.org/10.1038/s41598-024-51883-1.

[6] Loehe J, Zaeh M. A new approach to build a heat flux model of milling processes. Procedia CIRP 2014;24:7–12. http://dx.doi.org/10.1016/j.procir.2014.08.003.

[7] Altintas Y, Kersting P, Biermann D, Budak E, Denkena B, Lazoglu I. Virtual process systems for part machining operations. CIRP Ann 2014;63(2):585–605. http://dx.doi.org/10.1016/j.cirp.2014.05.007.

[8] Bleicher F, Biermann D, Drossel W-G, Moehring H-C, Altintas Y. Sensor and actuator integrated tooling systems. CIRP Ann 2023;72(2):673–96. http://dx.doi.org/10.1016/j.cirp.2023.05.009.

[9] Denkena B, Boujnah H. Feeling machines for online detection and compensation of tool deflection in milling. CIRP Ann 2018;67(1):423–6. http://dx.doi.org/10.1016/j.cirp.2018.04.110.

[10] Denkena B, Boujnah H. Feeling machines for online detection and compensation of tool deflection in milling. CIRP Ann 2018;67(1):423–6. http://dx.doi.org/10.1016/j.cirp.2018.04.110.

[11] Ratchev S, Liu S, Huang W, Becker AA. Machining simulation and system integration combining FE analysis and cutting mechanics modelling. Int J Adv Manuf Technol 2007;35(1):55–65. http://dx.doi.org/10.1007/s00170-006-0700-6.

[12] Denkena B, Bergmann B, Stoppel D. Tool deflection compensation by drive signal-based force reconstruction and process control. Procedia CIRP 2021;104:571–5. http://dx.doi.org/10.1016/j.procir.2021.11.096.

[13] Evers L, Müller M, Möller C, Brouschkin A, Dege JH. Control loop based dimensional error compensation for milling of near-net-shaped, thin-walled structures. In: Kohl H, Seliger G, Dietrich F, Vien HT, editors. Decarbonizing value chains. Cham: Springer Nature Switzerland; 2025, p. 399–407.

[14] Alzugaray-Franz R, Diez E, Villaverde M, Vizán A. Indirect measurement of process parameters in peripheral end milling based on acoustic emission signals. Measurement 2024;234:114801. http://dx.doi.org/10.1016/j.measurement.2024.114801.

[15] Luo M, Liu D, Luo H. Real-time deflection monitoring for milling of a thin-walled workpiece by using PVDF thin-film sensors with a cantilevered beam as a case study. Sensors 2016;16(9). http://dx.doi.org/10.3390/s16091470.

[16] Friedrich M, Thorenz B, Doepper F. Investigation of the influence of sensorized tool holders on dynamic properties and manufacturing results during milling. J Manuf Mater Process 2025;9(10). http://dx.doi.org/10.3390/jmmp9100342.

[17] Choi J-G, Yang M-Y. In-process prediction of cutting depths in end milling. Int J Mach Tools Manuf 1999;39(5):705–21. http://dx.doi.org/10.1016/S0890-6955(98)00067-4.

[18] Kienzle O, Victor H. Bestimmung von Kräften an Werkzeugmaschinen. 1952, VDI-Z 94.

[19] Faouzi J, Janati H. Pyts: A python package for time series classification. J Mach Learn Res 2020;21(46):1–6, URL http://jmlr.org/papers/v21/19-763.html.

[20] Pekelharing AJ. The exit failure of cemented carbide face milling cutters part I — Fundamentals and phenomenae. CIRP Ann 1984;33(1):47–50. http://dx.doi.org/10.1016/S0007-8506(07)61377-8.

[21] Virtanen P, Gommers R, Oliphant. SciPy 1.0: Fundamental algorithms for scientific computing in python. Nature Methods 2020;17:261–72. http://dx.doi.org/10.1038/s41592-019-0686-2.

[22] Wimmer S, Zaeh MF. The prediction of surface error characteristics in the peripheral milling of thin-walled structures. J Manuf Mater Process 2018;2(1). http://dx.doi.org/10.3390/jmmp2010013.